ELSEVIER

Numerical simulation of liquid phase electro-epitaxial selective area growth

M. Khenner[a,*], R.J. Braun[b]

[a]Department of Mathematics, State University of New York at Buffalo, Buffalo, NY 14260-2900, USA
[b]Department of Mathematical Sciences, University of Delaware, Newark, DE 19716, USA

Abstract

A computational model for semiconductor crystal growth on a partially masked substrate under simplified liquid phase electroepitaxy conditions is developed. The model assumes isothermal diffusional growth, which is enhanced by applied DC current through crystal-solution interface. A finite-difference, front-tracking method is used to numerically evolve the interface. Computed examples show strong influence of the electromigration on growth rates in vertical and lateral directions and the dependence of growth on electrical resistance of mask material, and on the wetting contact angle.

© 2005 Elsevier B.V. All rights reserved.

1. Introduction

In this paper, we numerically study crystal growth on a patterned masked substrate. When the substrate is partially masked, the epitaxial crystals may be useful for process diagnostics or for electronic devices "as grown" [1–3]. In the growth process we model here, the semiconductor crystal to be grown is deposited on a substrate which is exposed to the liquid through etched windows in a mask (e.g., a deposited metal or dielectric thin film). Liquid phase is assumed to be a mixture (solution) of a molten metal (solvent, say Bi) and two or more components of which the epitaxial film is to be formed (solute, say GaAs particles). Crystal growth techniques which employ patterned substrates fall in the category of so-called selective area growth (SAG) techniques.

---

*Corresponding author.

E-mail address: mkhenner@nsm.buffalo.edu (M. Khenner).

We consider growth from liquid phase which is influenced by passing a DC current through the interface between the solid and liquid phases. Such crystal growth technique is called liquid phase electroepitaxy (LPEE) when growth is on regular, non-patterned substrates. LPEE was studied intensively during the last two decades, see for example [4–8]. Among physical processes which may contribute to LPEE crystal growth are diffusion, electromigration, convection, heat transfer, and thermoelectric effects, e.g. Joule heat, Peltier, Thompson, DuFour, Soret and Seebeck effects.

In contrast to conventional LPEE, LPEE on masked patterned substrate is studied much less. We will refer to the latter process as LPEESAG. Experimental studies of LPEESAG are described, for example, in Refs. [9–12]. In contrast to the number of computational studies carried out for LPEE, there are relatively few theoretical and computational studies of LPEESAG. A one-dimensional diffusional model with electromigration [13] was studied by Sakai et al., and a quasi-two-dimensional (2D) model was developed subsequently [14]. Their 2D model based the calculations on a representative crystal shape and they concluded that the relative growth rate of the crystal over the mask was increased due to surface diffusion of material from the mask in comparison with the direction perpendicular to the mask. Their model did not take into account the crystal-solution interface evolution; that is, the changing crystal shape during growth did not affect the diffusion fields around the crystal and vice versa. The emphasis in this paper is on developing a simple model and numerical method which potentially is capable of handling the evolution and interaction of the crystal growth, electric potential and the diffusion fields in LPEESAG.

In our model, the diffusion of solute on both sides of the interface, the electric potential, and the properties of the boundaries and the crystal-solution interface determine the evolution of the interface. The mathematical problem is solved by way of a modification of the approach of Juric and Tryggvason for dilute binary alloy solidification [15]. Some details of their approach appear in the paper on solidification from a pure substance [16].

The paper proceeds as follows. In Section 2, a simplified model of LPEESAG (that includes only diffusion and electromigration as two major processes) is presented. The numerical method is briefly discussed in Section 3. Results of the modeling are presented in Section 4 and discussed in Section 5.

2. Mathematical model

In this section, we describe the mathematical model which is an initial/boundary value problem for a system of coupled partial differential equations; the equations describe evolution of concentration of solute and the electric potential in the liquid solution and in the crystal.

Fig. 1 shows a sketch of the mathematical situation; we examine the growth behavior on a partial cross-section which is a line segment extending from the center line of one mask surface at $x' = -\ell$ to the center of the adjacent open stripe at $x' = L$. The mask region is $[-\ell, 0]$; the stripe region is $[0, L]$. We assume the surface behavior is constant in the perpendicular direction since we are interested in modeling the regular case of crystal growth in long, parallel and straight etched stripes [2,3,9–12]; thus the model operates in two
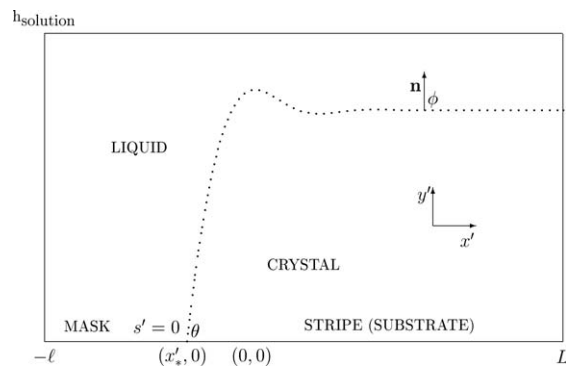

Fig. 1. A sketch of the mathematical situation. The free surface of the growing crystal (curve in two dimensions) is sketched such that a crystal overgrowth onto the mask is shown. ϕ is the angle that the unit normal, **n**, makes with the horizontal axis; **n** points into the liquid phase. θ is the angle that the crystal surface makes with mask surface. This angle is assumed constant for given material system (see text). The interface is parametrized by arc length, s'.

dimensions. For simplicity, it is also assumed that mask thickness is zero.

A starting point for our model is system of equations derived in Ref. [17], the second of three papers considering the stability of directional solidification of binary alloy in the presence of the electric field [18,19]. Alternatively, in Ref. [7], authors used irreversible thermodynamics to obtain a general formulation for the problem including fluid motion. We refer the reader to [17] for assumptions and details of the derivation. Elastic stresses in the crystals (which may arise, for example, due to lattice mismatch between substrate and crystal materials) are ignored, and constant supply of semiconductor material from the source located at the top of the solution is assumed (that is, the solution is never depleted). We also assume, specifically for SAG, that there is no interaction between growing (out of each stripe) crystals since stripes are spaced sufficiently far apart.

In the solution, we designate variables with a subscript L; in the crystal, variables are designated with a subscript S. Primes denote dimensional variables.

Assuming that the interfacial temperature is very closely approximated by the equilibrium melting temperature of pure material, T_M (at least for LPEE of GaAs-like compound semiconductors), we investigate an isothermal model. Assume that diffusion of the solute concentration and the electromigration are important in both phases. Under isothermal conditions, the problem formulated in Ref. [17] greatly simplifies to the following problem:

$$\frac{\partial c'_L}{\partial t'} = D_L \nabla^2 c'_L - \frac{u_L}{\sigma_L} \mathbf{I}'_L \cdot \nabla c'_L, \tag{2.1}$$

$$\nabla^2 \psi'_L = 0, \tag{2.2}$$

$$\frac{\partial c'_S}{\partial t'} = D_S \nabla^2 c'_S - \frac{u_S}{\sigma_S} \mathbf{I}'_S \cdot \nabla c'_S, \tag{2.3}$$

$$\nabla^2 \psi'_S = 0. \tag{2.4}$$

Here, c'_L (c'_S) is solute concentration and ψ'_L (ψ'_S) is electrical potential in the liquid (solid) phase; D_L (D_S) and u_L (u_S) are solute diffusivity and

electric mobility, and σ_L (σ_S) are electrical conductivities of liquid (solid) phases. $\mathbf{I}'_L = -\sigma_L \nabla \psi'_L$ and $\mathbf{I}'_S = -\sigma_S \nabla \psi'_S$ are current densities.

2.1. Interfacial conditions

At the crystal-solution interface, both the potential and the current are continuous:

$$\psi'_L = \psi'_S, \tag{2.5}$$

$$\sigma_L \mathbf{n} \cdot \nabla \psi'_L = \sigma_S \mathbf{n} \cdot \nabla \psi'_S. \tag{2.6}$$

We may take the view that the normal speed of the interface, V'_n, is set by a modified Gibbs–Thomson condition

$$V'_n / \mu = m c'_L - \Gamma \mathscr{K}', \tag{2.7}$$

where m is the liquidus slope, Γ is the capillary parameter, μ is the kinetic coefficient (interface mobility), and $\mathscr{K}'$ is the curvature of the interface.

The solute must be conserved at the interface via

$$D_L \mathbf{n} \cdot \nabla c'_L - D_S \mathbf{n} \cdot \nabla c'_S + (1-k) c'_L V'_n$$
$$= \frac{u_L c'_L}{\sigma_L} \mathbf{I}'_L \cdot \mathbf{n} - \frac{u_S c'_S}{\sigma_S} \mathbf{I}'_S \cdot \mathbf{n}, \tag{2.8}$$

where k is the segregation coefficient. k is defined as $k = c'_S / c'_L$ where the concentrations are evaluated at the interface; k measures how much of the solute is rejected upon formation of a crystal.

2.2. Other boundary conditions

We first discuss the boundary conditions on the electric potential. In the solution, a specified current density I_0 enters the top of the solution (top of computational domain) at $y' = h_{solution}$ (ref. Fig. 1); in accord with regular convention, we mean current of *positive* particles (e.g., electron current is in $-\mathbf{I}$ direction). We then have

$$\mathbf{I}'_L = I_0 \mathbf{n}_t = -\sigma_L (\partial \psi'_L / \partial y') \mathbf{n}_t, \tag{2.9}$$

where $\mathbf{n}_t$ is the unit outward normal to the top boundary of the computational box. On either vertical side of the computational box, at $x' = -\ell$ and $x' = L$, we have the symmetry conditions

$$\partial \psi'_L / \partial x' = \partial \psi'_S / \partial x' = 0. \tag{2.10}$$

At the bottom of the box at $y' = 0$ we must take into account the possibility of overgrowth onto the mask, as well as the possibility for the masking material to be either dielectric (say, SiO$_2$) or conductive (tungsten [10]). We therefore adopt the simplest model, as follows. Over the masked portion of the substrate at $[-\ell, 0)$, we impose

$$\mathbf{I}'_L = \mathbf{I}'_S = -\alpha I_0 \mathbf{n}_b, \tag{2.11}$$

here $\mathbf{n}_b$ is the unit outward normal to the bottom boundary of the computational box. Over the stripe region $[0, L]$, we impose

$$\mathbf{I}'_S = -(1 - \alpha) I_0 \mathbf{n}_b. \tag{2.12}$$

α is a prescribed constant. Choosing $0 \leqslant \alpha \leqslant 0.5$ allows to effectively vary the electrical resistance of the masking layer. The limiting cases are: (i) $\alpha = 0$ corresponds to dielectric mask. Thus in this case there is no electron current entering the masked portion of the substrate from the liquid phase, and electromigration over the mask vanishes. (ii) $\alpha = 0.5$ stands for the situation when the masked and open regions of the substrate support equal fractions of the current density I_0. That is possible only when the mask is conductive, as in Mauk and Curran [10], for example.

We now discuss the concentration boundary conditions. At $y' = h_{\text{solution}}$, the concentration is prescribed: $c_L = c_\infty$. On vertical sides of the box, $\partial c'_L / \partial x' = \partial c'_S / \partial x' = 0$ due to symmetry. At the bottom of the box,

$$\frac{\partial c'_L}{\partial y'} - \frac{u_L}{\sigma_L D_L} c'_L \mathbf{I}'_L = 0, \tag{2.13}$$

$$\frac{\partial c'_S}{\partial y'} - \frac{u_S}{\sigma_S D_S} c'_S \mathbf{I}'_S = 0, \tag{2.14}$$

meaning that there is no mass flux through the mask and the stripe.

We also have the constant equilibrium angle θ which the crystal surface forms with the mask at the contact point $(x'_*, 0)$, as given by the Young–Dupré equation

$$\cos \theta = \frac{\gamma_{ms} - \gamma_{cm}}{\gamma_{cs}}. \tag{2.15}$$

Here, γ_{ms}, γ_{cm} and γ_{cs} are constant (independent of orientation) energies of the mask-solution, crystal-mask and crystal-solution interfaces.

2.3. Physical parameters and nondimensional problem

Representative physical parameters for LPEE-SAG of GaAs-like semiconductors are given in Table 1. Self-diffusion in III–V compound semiconductors is, as a rule, very slow. For instance, the diffusion coefficients of Ga and As in GaAs are of the order 10^{-14}–10^{-15} cm^2/s at $1025\,^\circ$C [20, p. 197], and thus value of D_S in Table 1 is overestimated. However, for III–V systems there are cases when self-diffusion is not as slow. For instance, values for diffusion prefactors and activation energies cited on p. 202 of [20] for In

Table 1
Physical parameters for a GaAs-like material; we are not attempting to exactly model GaAs. We choose $T_M = 1073\,$K which is (i) close to the melting point of As (the latter is 1090 K) and (ii) coincides with the typical growth temperature (liquidus or saturation temperature) [8]

Parameter	Value at $\approx 800\,^\circ$C	Units	Reference
σ_L	2.5×10^4	$\Omega^{-1}\,$cm^{-1}	[8]
σ_S	4000	$\Omega^{-1}\,$cm^{-1}	See text
D_L	4×10^{-5}	cm$^2\,$s^{-1}	[8]
D_S	4×10^{-7}	cm$^2\,$s^{-1}	See text
m	2.45×10^{-4}	K at%$^{-1}$	[8]
k	10^{-4}	—	[21]
u_L	0.027	cm$^2\,$V$^{-1}\,$s^{-1}	[8]
u_S	1.1×10^4	cm$^2\,$V$^{-1}\,$s^{-1}	[22]*
μ	200	cm s$^{-1}\,$K^{-1}	*
γ	700	ergs/cm^2	[9]
L_V	1000	J cm^{-3}	*
$\Gamma = \gamma T_M / L_V$	7.5×10^{-5}	cm K	*
L	5×10^{-4}	cm	[9]
ℓ	5×10^{-3}	cm	[9]
h_{solution}	1	cm	[9]
I_0	10	A cm^{-2}	[8,9]
c_∞	2.23×10^{-2}	%	[8]
θ	$0^\circ - 180^\circ$		—

L_V is latent heat of fusion. The values marked with an asterisk (*) are assumed because reliable data for semiconductors is difficult to find. Also note that for the same reason we use value of u_S which corresponds to *electron* mobility and not to solute electric mobility.

and As diffusion in InAs translate into self-diffusion coefficient of the order $10^{-11}\,\mathrm{cm}^2/\mathrm{s}$ for $T = 900\,^\circ\mathrm{C}$. Impurities may diffuse even faster, e.g. the typical diffusion coefficient of Zn in InAs is of the order $10^{-7}\,\mathrm{cm}^2/\mathrm{s}$ for $T = 800\,^\circ\mathrm{C}$. Taking this into account, we believe there is justification for using larger D_S; another reason is that, within the framework of two-sided model the numerical computations are easier to perform if the coefficients of equation do not differ by many orders of magnitude. We also wish to have the possibility of taking into account diffusion in the solid phase, as this may be required for modeling other groups of semiconductors. Note also that the conductivity in the solid is 100 times larger than the value of $40\,\Omega^{-1}\,\mathrm{cm}^{-1}$ given by Ref. [8]; we use this value also to avoid large ratio of conductivities in order to reduce the computational time needed to iteratively solve the two-phase analog of Eqs. (2.2), (2.4) which is Eq. (A.8), see Appendix A (and sometimes, to avoid divergence of iterations in multigrid cycle). The code MUDPACK [23] (available from NETLIB) is used for the solution of the Eq. (A.8).

Despite that all results presented in this paper are obtained using artificially large values of D_S and σ_S, we show in Fig. 9 two cases of computation with $D_\mathrm{S} = 10^{-14}\,\mathrm{cm}^2/\mathrm{s}$ and $\sigma_\mathrm{S} = 40\,\Omega^{-1}\,\mathrm{cm}^{-1}$. The discussion of this figure is included in the end of the Section 4.

We nondimensionalize the problem as follows. All lengths are scaled with the width L of substrate (stripe) region; then, the computational domain is over $-d \leqslant x \leqslant 1$, $0 \leqslant y \leqslant h$, where $d = \ell/L$, $h = h_{\mathrm{solution}}/L$. The masked substrate occupies $-d \leqslant x < 0$, $y = 0$, and the stripe occupies $0 \leqslant x \leqslant 1$, $y = 0$. The time is scaled with L^2/D_L, the current density with the applied value I_0, the concentration with the far field boundary value c_∞. We will also eliminate the current density as a variable in favor of gradients of the electric potential ψ. The nondimensional parameters are shown in Table 2.

The nondimensional equations in the bulk of either phase read:

$$\frac{\partial c_\mathrm{L}}{\partial t} = \nabla^2 c_\mathrm{L} + U_\mathrm{L} \nabla \psi_\mathrm{L} \cdot \nabla c_\mathrm{L}, \tag{2.16}$$

Table 2
Nondimensional parameters

Parameter	Value
$U_\mathrm{L} = u_\mathrm{L} I_0 L/(\sigma_\mathrm{L} D_\mathrm{L})$	10^{-4}
$U_\mathrm{S} = u_\mathrm{S} I_0 L/(\sigma_\mathrm{S} D_\mathrm{L})$	300
$D = D_\mathrm{S}/D_\mathrm{L}$	10^{-2}
$\Sigma = \sigma_\mathrm{S}/\sigma_\mathrm{L}$	0.1
$M = m c_\infty/T_\mathrm{M}$	5×10^{-9}
$G = \Gamma/(L T_\mathrm{M})$	10^{-4}
$\xi_0 = \mu D_\mathrm{L}/(L T_\mathrm{M})$	1.5×10^{-2}
$d = \ell/L$	10
$h = h_{\mathrm{solution}}/L$	2×10^3

$$\nabla^2 \psi_\mathrm{L} = 0, \tag{2.17}$$

$$\frac{\partial c_\mathrm{S}}{\partial t} = D \nabla^2 c_\mathrm{S} + U_\mathrm{S} \nabla \psi_\mathrm{S} \cdot \nabla c_\mathrm{S}, \tag{2.18}$$

$$\nabla^2 \psi_\mathrm{S} = 0. \tag{2.19}$$

On the crystal-solution interface, we have

$$\psi_\mathrm{L} = \psi_\mathrm{S}, \tag{2.20}$$

$$\frac{\partial \psi_\mathrm{L}}{\partial n} = \Sigma \frac{\partial \psi_\mathrm{S}}{\partial n}, \tag{2.21}$$

$$V_\mathrm{n}/\xi = M c_\mathrm{L} - G \mathscr{K}, \tag{2.22}$$

$$\frac{\partial c_\mathrm{L}}{\partial n} - D \frac{\partial c_\mathrm{S}}{\partial n} + (1 - k) c_\mathrm{L} V_\mathrm{n}$$
$$= -U_\mathrm{L} c_\mathrm{L} \frac{\partial \psi_\mathrm{L}}{\partial n} + U_\mathrm{S} c_\mathrm{S} \frac{\partial \psi_\mathrm{S}}{\partial n}. \tag{2.23}$$

In Eq. (2.22), G is capillary parameter, ξ is interface mobility. $\partial/\partial n$ is directional derivative along $\mathbf{n}$. We allow for the anisotropy of ξ:

$$\xi = \xi_0 [1 + \varepsilon_\xi \cos(p\phi + \beta_\xi)], \tag{2.24}$$

where ξ_0 is mean value (ref. Table 2). The constant ε_ξ determines the degree of the anisotropy of ξ; value of p specifies the type of anisotropy (for example, $p = 4$ corresponds to four-fold anisotropy). ϕ is the angle that the unit normal to the interface makes with the horizontal axis, and β_ξ is the phase shift. For our numerical experiments, we take values for ε_ξ within [0,1) to avoid the ill-posedness of the evolution problem [24]. Mathematically sharp corners (missing orientations) on crystal surface are therefore excluded from

consideration. The anisotropy of the capillary parameter can be incorporated in the model in the similar fashion; however, this requires more complicated Herring condition [25] at the tri-junction crystal-mask solution. We did not attempt to include this anisotropy in this work.

The nondimensional boundary conditions are as follows. At $x = -d$ and 1, for $0 < y < h$, we have

$$\frac{\partial \psi_L}{\partial x} = \frac{\partial \psi_S}{\partial x} = \frac{\partial c_L}{\partial x} = \frac{\partial c_S}{\partial x} = 0. \qquad (2.25)$$

On $-d \leqslant x \leqslant 1$, $y = h$, we have

$$\frac{\partial \psi_L}{\partial y} = -1, \quad c_L = 1. \qquad (2.26)$$

On $-d \leqslant x < x_*$, $y = 0$, we have

$$\frac{\partial c_L}{\partial y} + U_L c_L \alpha = 0, \quad \frac{\partial \psi_L}{\partial y} = \alpha, \qquad (2.27)$$

on $x_* \leqslant x < 0$, $y = 0$,

$$\frac{\partial c_S}{\partial y} + U_S c_S \frac{(1+d)\alpha}{D\Sigma} = 0, \quad \frac{\partial \psi_S}{\partial y} = \frac{(1+d)\alpha}{\Sigma}, \qquad (2.28)$$

on $0 \leqslant x \leqslant 1$, $y = 0$,

$$\frac{\partial c_S}{\partial y} + U_S c_S \frac{(1+d)(1-\alpha)}{D\Sigma} = 0,$$

$$\frac{\partial \psi_S}{\partial y} = \frac{(1+d)(1-\alpha)}{\Sigma}. \qquad (2.29)$$

Finally, at $x = x_*$, $y = 0$, we have

$$\theta = \text{const.} \qquad (2.30)$$

3. Numerical method

We employ a method closely related to those developed by Tryggvason and coworkers, which was successfully applied to many problems in multiphase fluid flow (for a review, see [26]) and for alloy solidification [15]. Their method is a two-grid, front-tracking method. The field variables (concentration and electrical potential in our case) are resolved on 2D stationary, uniform, rectangular finite-difference grid. The interface is explicitly tracked by a separate grid of marker particles. The communications between grids are

done by a method that is known as the *immersed boundary technique* [27]. The zero-thickness interface is approximated by a smooth distribution function which spreads the interface over a few grid points surrounding the interface. The distribution function also interpolates the field variables to the interface.

In Appendix A, we describe in detail the modification of the approach of Juric and Tryggvason for alloy solidification [15] that is applied to the present problem.

4. Results

In this section, our goal is to demonstrate how changes of certain system parameters influence the crystal surface shape and the growth rates. Due to very large number of nondimensional parameters involved, we fix most of these parameters.

4.1. Isotropic surface properties

To study isotropic surface evolution under influence of the electric currents, we take $\varepsilon_\xi = 0$. We also take dielectric mask ($\alpha = 0$), and the contact angle $\theta = 60°$. Other values of parameters for this run were selected as in Table 2, with the exception of values for d and h, which were taken 0.4 and 1, respectively. Also, quotient $U_S/(D\Sigma)$ in Eqs. (2.28) and (2.29) is chosen small to the extent that allows for absence of destabilization near the contact line. The computation was done on a 192×192 grid. The small dimensions of the computational box were chosen to ensure high enough grid resolution, especially in the region near the contact point; simulations on much larger domains are possible but impractical, since grids of very large sizes are needed. The interfacial grid has 250 marker particles.

Fig. 2(a) shows crystal surface profiles at nondimensional times $t = 0$, 200, 400, 600, 800, 1000 for imposed current densities $I_0 = 0$, 2, $10 \, \text{A/cm}^2$ (values of U_L and U_S in Table 2 are recomputed every time I_0 is changed to a new value). Fig. 2(b) shows crystal height at the center of the stripe as function of time for these three runs. Firstly, as is evident from both figures, the
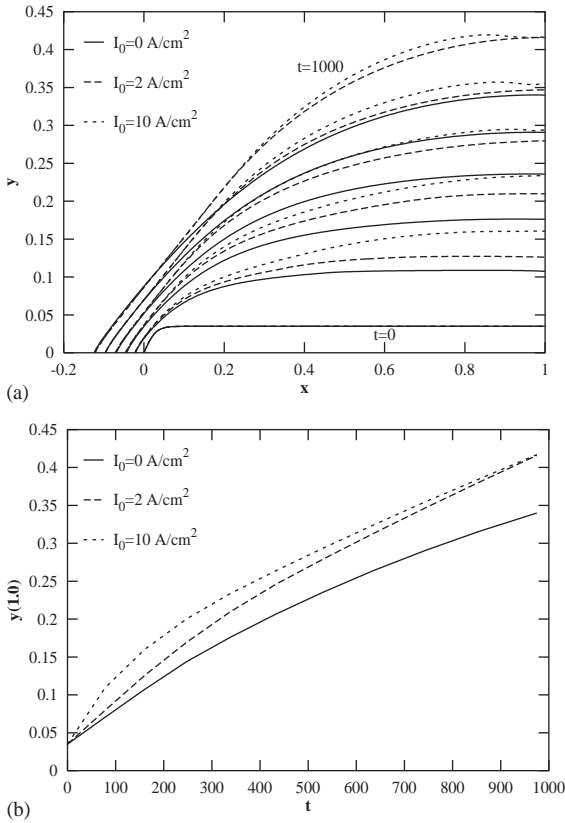
Fig. 2. Interface profiles (a) and crystal height in the middle of the stripe, (b) for different imposed current densities I_0. $\varepsilon_\xi = 0$ (no anisotropy), $\alpha = 0$, $\theta = 60°$.

electromigration enhances growth in the vertical direction, the enhancement being stronger for stronger currents. Notice some overgrowth on the mask. Due to numerical edge effect which sometimes is pronounced for high current densities (note the concave regions on dotted surface profiles near $x = 1$ in Fig. 2(a)), the dotted curve in Fig. 2(b) is less steep than expected. The increased computational accuracy there will eliminate this effect and make the dotted curve steeper. For the case of $I_0 = 2\,\text{A/cm}^2$, the growth rate is constant for $t > 500$, e.g. after the initial transient phase, while for the no-current case the growth is still in the transient phase up to $t = 1000$.

Fig. 3 shows contour plots of the concentration and electrical potential fields for $I_0 = 10\,\text{A/cm}^2$ case of the Fig. 2. In Fig. 3(a), note nearly vertical

bands of progressively decreasing concentration as one cuts across the solid from the contact point to the symmetry boundary (middle of the crystal). These vertical bands bend near the crystal surface, particularly near the contact point, to follow the local geometry there. There is clearly a gradient of concentration across the crystal that is developing as time goes on. A pronounced gradient in the solid develops because the electromigration in the solid phase is large compared to diffusion there; the nondimensional coefficient of the solid electromigration term is about four orders of magnitude larger than coefficient of the solid diffusion term, and about six orders of magnitude larger than the coefficient of the liquid electromigration term. These relative sizes explain the relatively rapid development of the concentration field in the solid phase.

Fig. 4 shows the cross-sections, at different times, of the potential in the entire domain by vertical line $x = 0.5$. The electrical potential curves exhibit smoothed bends at the interface location due to the change of the electrical conductivity from 1.0 in the liquid to $\Sigma = 0.1$ in the solid. The gradient of the potential is toward the substrate at $y = 0$, and therefore the electron current in the solution is also toward the substrate and growing crystal, promoting the electromigration mass flux in this direction. The latter results in the enhanced growth rate, as will be seen below.

4.2. Anisotropic surface properties

Fig. 5 shows crystal surface for $I_0 = 10\,\text{A/cm}^2$, $\varepsilon_\xi = 0.95$, $p = 4$, $\beta_\xi = 45°$, $\theta = 60°$ and two limiting values of α. We selected four-fold anisotropic interface mobility with the phase shift since our studies [28] of SAG from vapor indicated that under certain conditions such choice allows for the maximal lateral growth rate.

The comparison of Fig. 2(a) (dotted curves) and Fig. 5(a, b) shows that vertical growth rate is indeed decreased in the anisotropic case (by a little less than two times), and lateral growth rate is increased. Also, the vertical growth can be enhanced by decreasing α. That is, vertical growth rate is maximal if mask is dielectric ($\alpha = 0$) and thus no current enters the mask. The electro-
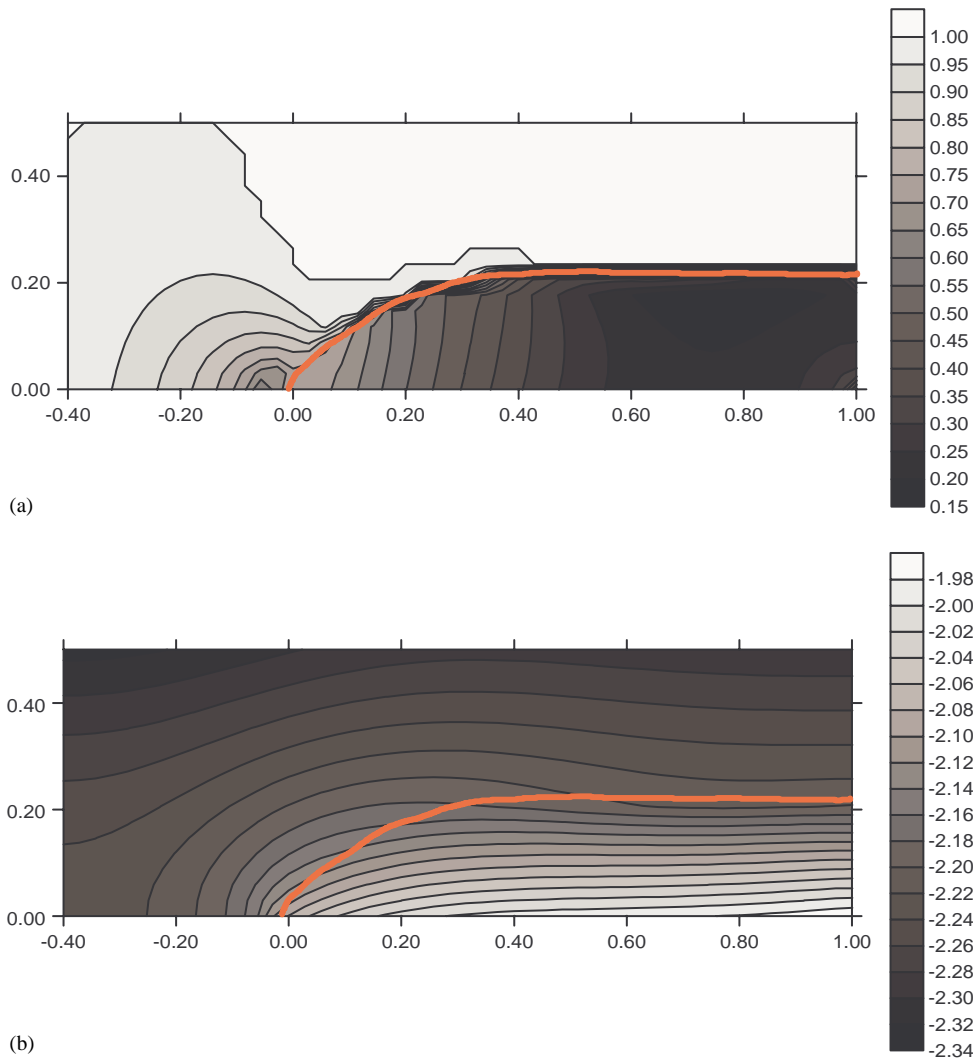
Fig. 3. Contour plots of (a) concentration field and (b) electric potential field at $t = 250$. Red curve on these plots shows the approximate (sketched by hand) location of the crystal-solution interface. See more comments about this figure and Fig. 9 in the Appendix B.

migration thus occurs predominantly above the stripe. The lateral growth rate is not affected by the change in mask resistance; however, that will change once the crystal poorly 'wets' the mask (see below). Also note that the crystals developed two slightly-curved surfaces resembling facets.

Fig. 6(a, b) demonstrate the electrical potential fields for the crystal growth shown in Fig. 5(a, b), respectively. For the insulating mask case (Fig. 6(a)), the gradient of the potential (and thus

the current) occurs predominantly above the stripe, forcing the electromigration that promotes the growth there; for the conductive mask case, (Fig. 6(b)) the current occurs more above the mask (where there is no crystal yet), and thus the growth on the stripe is slower. We view this result as a more self-consistent computation supporting and generalizing the conclusions of Sakai et al. [14].

Fig. 7(b, c) show electromigration-influenced anisotropic growth with $\theta = 120°$; the other parameters
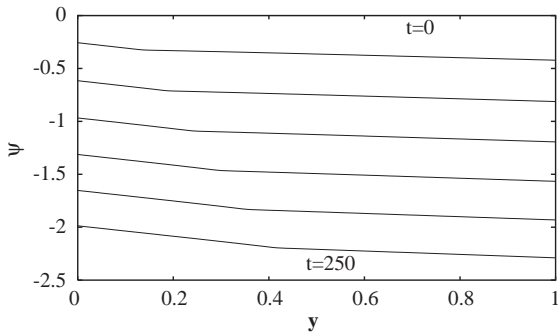
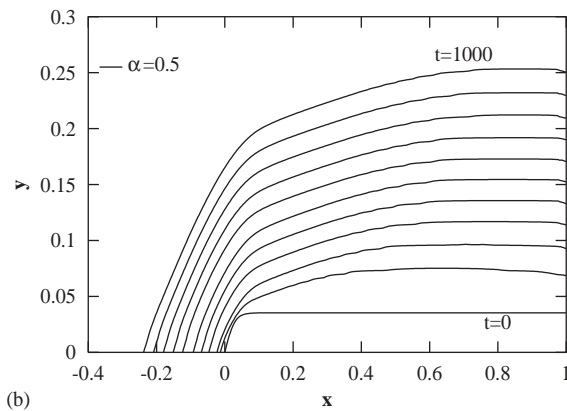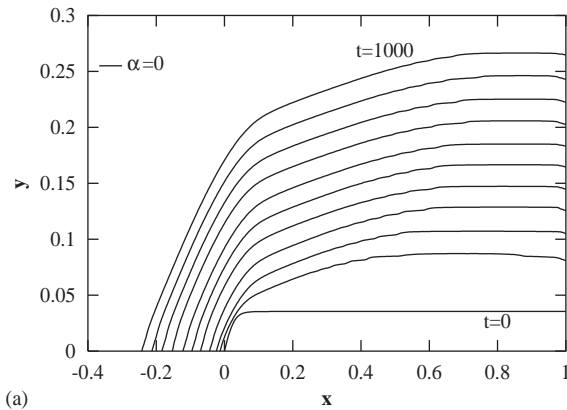Fig. 4. Evolution of the electrical potential along the line $x = 0.5$.

Fig. 5. Interface profiles for dielectric ((a), $\alpha = 0$) and conductive ((b), $\alpha = 0.5$) masks. $I_0 = 10\,\text{A/cm}^2$, $\varepsilon_\xi = 0.95$, $p = 4$, $\beta_\xi = 45°$ (four-fold anisotropic interface mobility), contact angle $\theta = 60°$.

are the same as for Fig. 5. Fig. 7(a) is included for comparison. As α changes, we see drastic changes in both film morphology and growth rates.

Fig. 7(b) shows results for $\alpha = 0$; only the neighborhood of the contact point is shown. The crystal grows fast vertically, and in this direction the growth is faster than in the isotropic, 'no current' case of Fig. 7(a); however, lateral overgrowth is extremely slow. Initially, crystal retracts on the stripe instead of overgrowing onto the mask. Physically, the retraction is possible due to melting back the substrate; however, we do not allow that in the model. The short retraction in Fig. 7(b) is solely due to the rearrangement of the interface from initial contact angle $\theta_0 = 60°$ to $\theta = 120°$. Once this equilibrium contact angle is achieved, the retraction stops and the direction of the contact point's lateral movement reverses to one on the mask. The retraction is generally present in other runs with $\theta > 90°$ (see, e.g. Fig. 7(a, c)) but is not shown on the graphs since it takes place very fast there.

Fig. 7(c) shows the $\alpha = 0.5$ case. In this case, the lateral growth rate is increased significantly at the expense of vertical growth; the overgrowth on the mask is almost completed by $t = 450$.

We also performed a simulation with $\theta = 150°$ (not shown); the vertical growth rate changed insignificantly compared to just discussed case of $\theta = 120°$, but lateral growth rate increased by a factor of 2.

Our last set of numerical experiments was conducted with reversed current, that is with current from the solution into the substrate ($I_0 < 0$). In a real crystal growth process, applying the current in this direction could result in dissolution of the crystal instead of growth [6], although in theory the reverse-direction current could be superimposed on a transient cooling of the solution to yield net growth. For our simple model, reversed current induces interfacial instability. Fig. 8(a, b) show this instability for the cases of isotropic growth on dielectric and conductive mask, respectively. It is obvious that the stability of the interface above the substrate is influenced by the degree of mask conductivity. In fact, making the mask conductive makes the instability less pronounced.

Finally, Fig. 9 shows *isotropic* computation with $U_S = 3 \times 10^4$, $D = 10^{-9}$, $\Sigma = 10^{-3}$. These values of nondimensional parameters correspond to
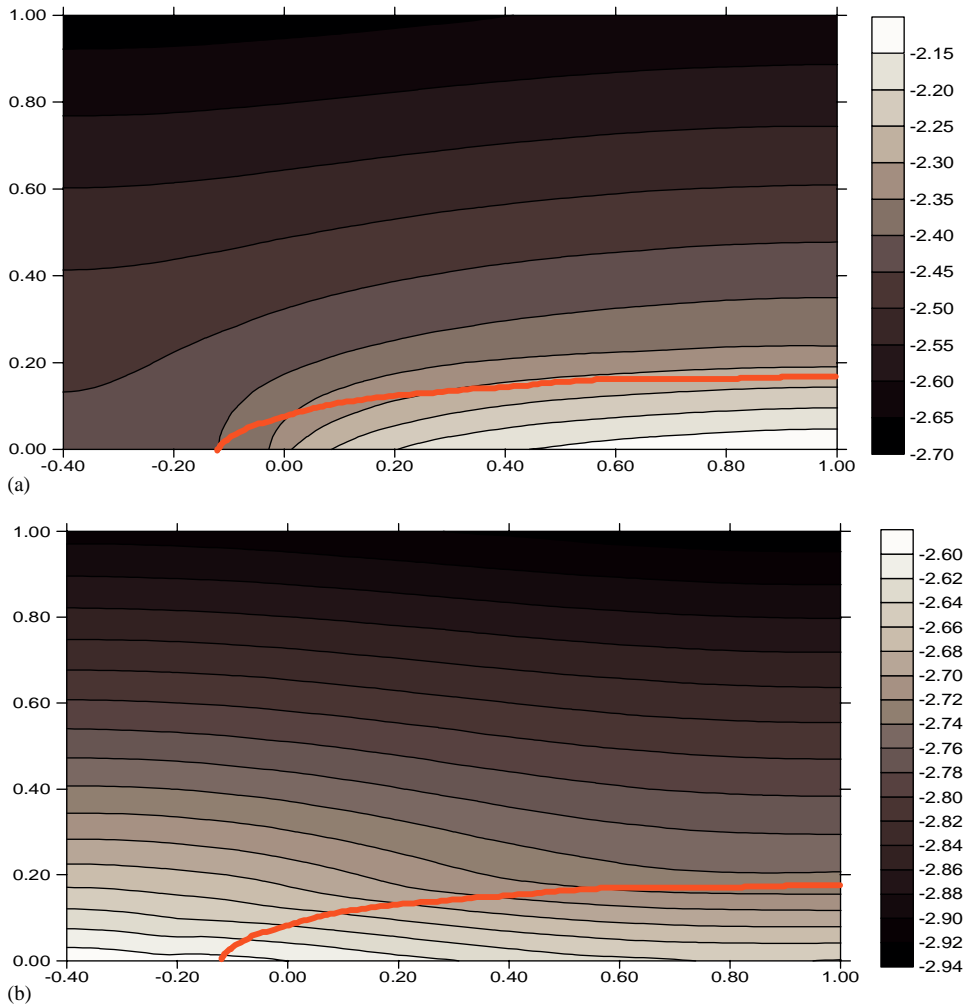
Fig. 6. Contour plots of the potential field at $t = 600$. (a) case of Fig. 5(a); (b) case of Fig. 5(b). See caption to Fig. 3 for meaning of the red curve.

diffusivity and electrical conductivity in the solid $D_S = 10^{-14} \, cm^2/s$, $\sigma_S = 40 \, \Omega^{-1} \, cm^{-1}$, respectively. Except for the anisotropy, interface profiles in Fig. 9(a) are quite similar to profiles in Fig. 5(b) obtained with larger values of D_S and σ_S; the former profiles are flatter in the central region. Same can be said about profiles in Figs. 9(b) and 7(c). All growth habits and differences mentioned above for the cases of weak and strong wetting of the substrate and mask conductivities hold in the case of more realistic values of D_S and σ_S. However it must be noted that absolute rate of

growth is faster in the case of small values of these parameters.

5. Discussion and conclusions

In this paper, a numerical method suitable for modeling electro-epitaxial selective area growth is introduced, and some examples of semiconductor thin film growth for a simplified LPEE process are computed. Although being very simple, the model we employed allows us to capture two phenomena
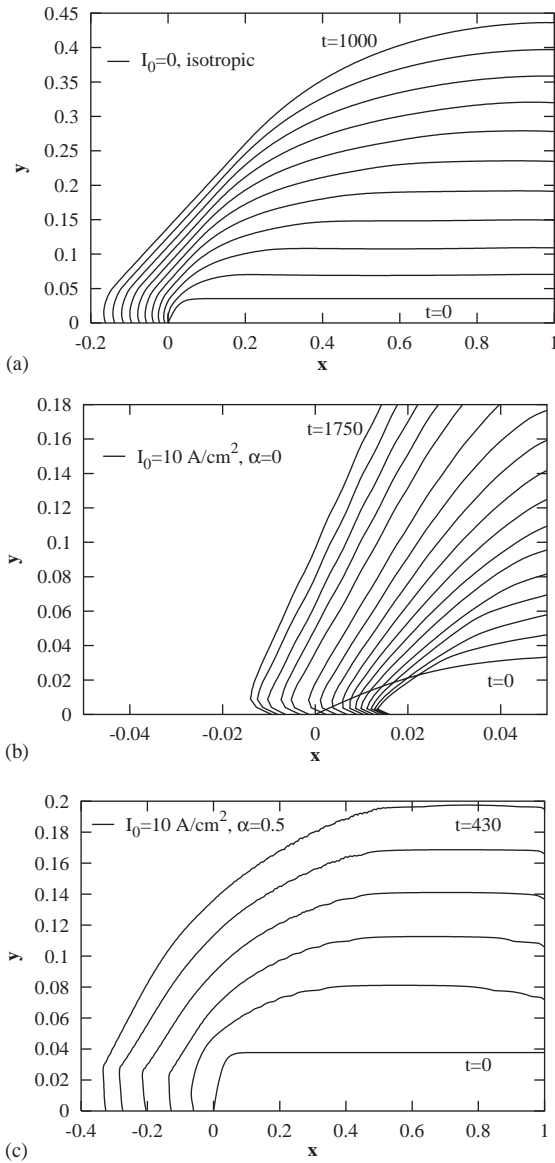
(a)

(b)

(c)

Fig. 7. Interface profiles for dielectric ((b), $\alpha = 0$) and conductive ((c), $\alpha = 0.5$) masks. $I_0 = 10\,\text{A/cm}^2$, $\varepsilon_\xi = 0.95$, $p = 4$, $\beta_\xi = 45°$, $\theta = 120°$. Isotropic evolution without the electromigration is shown for comparison in (a).

(a)

(b)

Fig. 8. Isotropic interface profiles for dielectric ((a), $\alpha = 0$) and conductive ((b), $\alpha = 0.5$) masks. $I_0 = -10\,\text{A/cm}^2$, that is in contrast to Figs. 2–7 the direction of the electromigration mass flux is from the mask/substrate into the bulk solution. $\varepsilon_\xi = 0$, $\theta = 60°$.

which occur in real crystal growth systems influenced by passing the electric current through them, namely diffusion and electromigration. We investigated growth rates in vertical and lateral directions as a function of (i) kinetic anisotropy, (ii) applied current density, (iii) masking layer
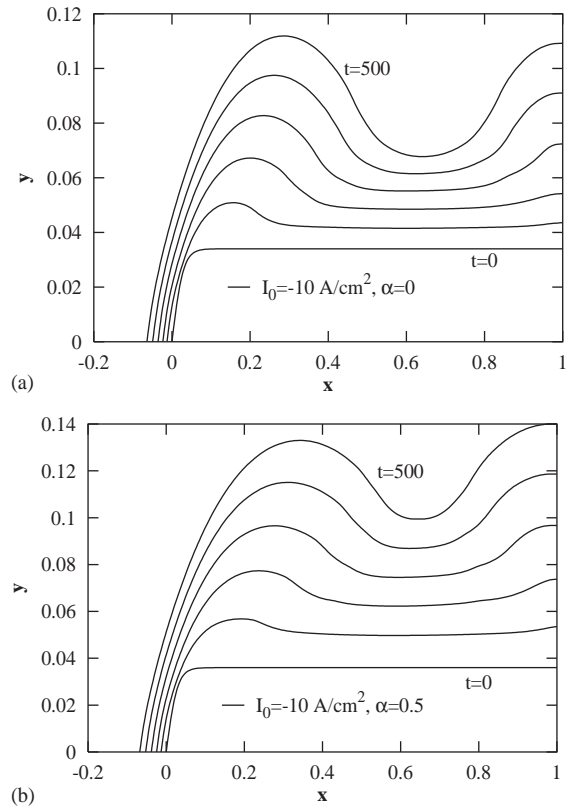
resistance, and (iv) the contact angle. It is found that the vertical growth rate can be greatly enhanced through the electromigration by directing the electric current through the mask/substrate into the solution. The enhancement is stronger with stronger currents and with the resistance of the mask. However, electromigration has little effect on lateral overgrowth onto the mask unless the crystal and mask materials are such that there is poor wetting of the mask by the crystal (i.e., large contact angle). In the large contact angle case, the rate of lateral overgrowth increases with the decrease of the mask resistance, and the vertical growth rate decreases accordingly. In our simulation, the passage of the electric current in the opposite direction (from the solution into the
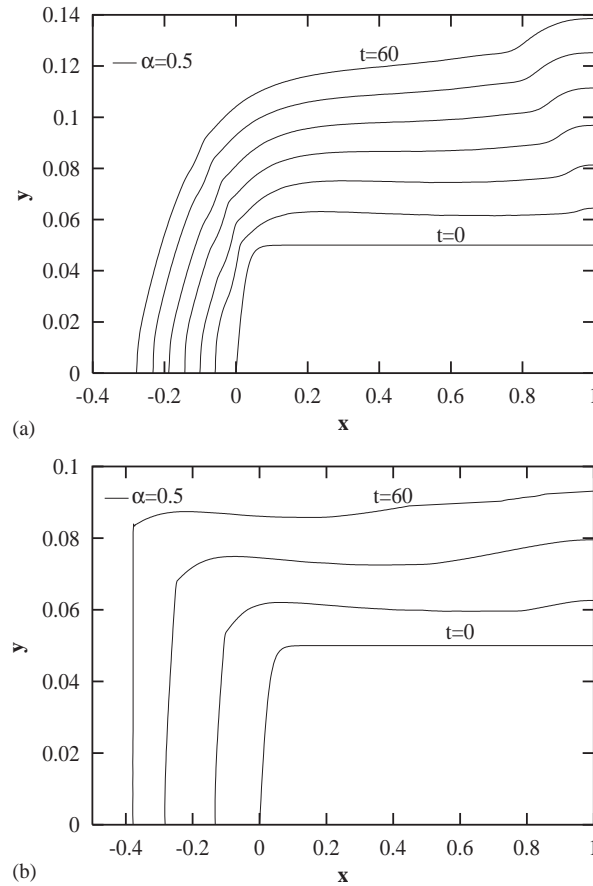
Fig. 9. Growth for conductive mask ($\alpha = 0.5$). $I_0 = 10\,\text{A/cm}^2$, $\varepsilon_\xi = 0$. For values of U_S, D, Σ see text. (a) $\theta = 60°$. The bulges near symmetry boundary is the numerical edge effect. (b) $\theta = 120°$.

mask/substrate) produces growth front instability, the extent of which may be decreased by directing current not only into the stripe, but also into the conductive mask. In real experiment, the contact angle can be controlled by appropriate choice of the mask material.

Our numerical results are consistent with experimental observations in LPEESAG systems [9,10,12]. In particular, the dependence of overgrowth rate on mask material was noticed in Ref. [9]. There, the increased overgrowth rate over tungsten masks (in comparison to silicon dioxide masks) was detected and attributed to the wetting phenomena. The films grown on tungsten masks all feature non-wetting behavior, e.g. contact angles larger than 90°. In Ref. [12] it was found that application of conductive tungsten mask

results in much wider and thinner electro-epitaxial layers than those grown on the substrates coated by dielectric film. The explanation for this experiment was provided based on the flow of current into the film, consistent with our modeling. As follows from the snapshots of the film, there is also little wetting of the substrate.

An analytical study of the stability of the binary alloy solidification in the electric field was carried out in Ref. [17]. Fig. 9 of their paper shows marginal stability curves in the plane (a, G_L/c_S), where a is nondimensional unstable wavenumber and G_L is temperature gradient at the interface for a germanium–gallium alloy. This alloy has thermophysical properties which resemble those of III–V compound we use as an example in this paper. The diagram is for the case of positive

growth speed and $I_0 < 0$. It is evident from this figure that there is a wide range of unstable wavenumbers ($0.05 < a < 5000$) for $G_L = 0$. On the other hand, as Fig. 8 of Ref. [17] indicates, there is even wider range of unstable wavenumbers for $I_0 > 0$, $G_L = 0$ case. Recall that we did not detect instabilities for $I_0 > 0$ case. The explanation of this contradiction can probably be found in Fig. 5 of Ref. [17]. There, two marginal stability curves are presented in $(V, G_L/c_S)$ coordinates, one for $I_0 > 0$ and another one for $I_0 < 0$ case. While it is not clear from this graph how the curves would look for very small V, it can be observed that for realistic values of V and nonzero G_L the marginal stability boundaries are straight, inclined parallel lines with narrow gap between them. It can happen that point $(V_*, (G_L/c_S)_*)$ corresponding to the particular realization of the growth falls in between these stability lines, in which case growth with $I_0 > 0$ will be stable and growth with $I_0 < 0$ will be unstable. It should be noted that formulation of the problem in Ref. [17] differs from our formulation in that there two semi-infinite regions are considered, diffusion in liquid phase only is accounted for (no diffusion in the solid), and temperature gradients are present (our formulation is isothermal). Stability analysis was also carried out in Ref. [29], but all the results are given there in terms of the temperature gradient and that makes it difficult to apply them to our model.

Acknowledgements

Appendix A. Numerical method

In this section, we outline the modification of the approach of Juric and Tryggvason for alloy solidification [15] to the current problem.

A.1. Reformulation of governing equations

To simplify numerical solution, we first restate the mass transport on both sides of the interface with a single equation [15]. To do this, we rescale the concentration, the diffusion coefficients and the electromigration coefficients, viz.,

$$\tilde{C} = \begin{cases} c_S/k & \text{in the solid,} \\ c_L & \text{in the liquid,} \end{cases} \qquad (A.1)$$

$$\tilde{D} = \begin{cases} Dk & \text{in the solid,} \\ 1 & \text{in the liquid} \end{cases} \qquad (A.2)$$

and

$$\tilde{U} = \begin{cases} U_S k & \text{in the solid,} \\ U_L & \text{in the liquid.} \end{cases} \qquad (A.3)$$

We then replace Eqs. (2.16) and (2.18) by

$$\frac{\partial \tilde{C}}{\partial t} = \nabla \cdot (\tilde{D}\nabla\tilde{C}) + \tilde{U}\nabla\psi \cdot \nabla\tilde{C}$$
$$+ \int_A \tilde{C}_f(1-k)V_n\delta(\mathbf{x} - \mathbf{x}_f)\,\mathrm{d}A. \qquad (A.4)$$

Note that in (A.4), $\tilde{C}$ is continuous across the interface. Also, ψ is the electric potential defined throughout the domain. ψ need not be rescaled because it is already continuous across the interface, ref. Eq. (2.20). The last term is an integral over the interface between the solid and the liquid, which must be tracked. This integral accounts for rejection or absorption of solute at the interface due to the difference in miscibility of the solution components in the liquid and solid. The subscript f designates a quantity evaluated at the interface, so that $\tilde{C}_f = \tilde{C}(\mathbf{x}_f(t))$ is the value of the transformed concentration at the interface. $\delta(\mathbf{x} - \mathbf{x}_f)$ is a 2D delta function which is non-zero only at the interface where $\mathbf{x} = \mathbf{x}_f$. Obviously, the integral source term is also nonzero only at the interface. On a 2D grid, the delta function is approximated in a standard way using Peskin's distribution function F_{ij} [30]. In the limit of vanishing interface thickness, Eq. (A.4) can be shown to recover the interfacial mass balance condition (2.23). $k = C_S(\mathbf{x}_f(t))/C_L(\mathbf{x}_f(t))$ is assumed to be constant as in [15].

In order to compute with Eq. (A.4), we must smooth the still-discontinuous $\tilde{D}$ and $\tilde{U}$ across the interface. To do this, we define

$$\hat{D} = (kD - 1)\rho(\mathbf{x}) + \frac{1 + kD}{2}, \tag{A.5}$$

$$\hat{U} = (kU_{\mathrm{S}} - U_{\mathrm{L}})\rho(\mathbf{x}) + \frac{U_{\mathrm{L}} + kU_{\mathrm{S}}}{2}, \tag{A.6}$$

where $\rho(\mathbf{x})$ is the material indicator function, which is -0.5 in the bulk liquid and 0.5 in the bulk solid, and which has a smooth, thin transition layer around the interface. The interface is, therefore, a zero level contour of $\rho(\mathbf{x})$. The indicator function is updated every time step given the location of the interface. For now, we replace $\tilde{D}$ and $\tilde{U}$ in Eq. (A.4) with $\hat{D}$ and $\hat{U}$ to obtain, finally, the equation which must be solved on 2D grid, everywhere in the computational box:

$$\frac{\partial \tilde{C}}{\partial t} = \nabla \cdot (\hat{D}\nabla\tilde{C}) + \hat{U}\nabla\psi \cdot \nabla\tilde{C} + \int_A \tilde{C}_f(1 - k)V_{\mathrm{n}}\delta(\mathbf{x} - \mathbf{x}_f)\,\mathrm{d}A. \tag{A.7}$$

We also must solve

$$\nabla \cdot \hat{\sigma}\nabla\psi = 0, \tag{A.8}$$

where

$$\hat{\sigma} = (\Sigma - 1)\rho(\mathbf{x}) + \frac{1 + \Sigma}{2} \tag{A.9}$$

is the smoothed electrical conductivity.

The fully specified mathematical problem consists of five parts: (i) Eqs. (A.5)–(A.9); (ii) associated problem for $\rho(\mathbf{x})$ (see below), (iii) the evolution law for the interface,

$$\frac{\mathrm{d}\mathbf{x}_f}{\mathrm{d}t} = V_{\mathrm{n}}, \tag{A.10}$$

(iv) interfacial and boundary conditions (2.20)–(2.30), (v) initial conditions for the concentration, electrical potential and interface position (specified below). Note that since the interface is tracked, we can regain the original concentration, diffusivity and electric mobility fields from the known position of the interface by, for example,

$$C = \frac{\tilde{C} + k\tilde{C}}{2} + (k\tilde{C} - \tilde{C})\rho(\mathbf{x}), \tag{A.11}$$

etc.

A.2. Discretization

Spatial derivatives in Eqs. (A.7), (A.8) are discretized using centered, second order finite differences. One-sided finite differences are used where needed to compute derivatives at the boundaries of the computational box. Second order finite differences are also used for the computation of the curvature of the interface, given Cartesian coordinates of marker particles and parameter (arclength) along the interface. For details on parametrization, see [31]. Time derivatives in Eqs. (A.7), (A.10) are approximated by the forward Euler method. We therefore have an explicit, forward-in-time-central-in-space finite difference scheme.

A.3. Treatment of the indicator function

As suggested in Ref. [30], the computation at every time step of $\rho(\mathbf{x})$ (for a closed curve) involves computation of Peskin's distribution function and solution of the Poisson equation for $\rho(\mathbf{x})$. In our case, the interface is open curve, and therefore it was necessary to modify the method of computing $\rho(\mathbf{x})$ to account for the local geometry of the interface near the contact point $(x_*(t), 0)$. These modifications are described elsewhere [32]. Also note that method of Ref. [30] has been extended to an open curve in the context of a liquid drop spreading on a substrate by Ref. [33].

A.4. Initial conditions for the interface shape $y = y(x)$, concentration field $\tilde{C}$ and potential ψ

The initial interface is a hyperbolic tangent curve which makes angle θ_0 with the mask at contact point:

$$y(x, 0) = y_0 \tanh\left(x \frac{\tan\theta_0}{y_0}\right), \quad 0 \leqslant x \leqslant 1, \tag{A.12}$$

where y_0 gives the small initial elevation of the surface at $x = 1$. For the simulations we take $y_0 = 0.04$ and $\theta_0 = \theta$ if $\theta < 90°$. If $\theta > 90°$, we take θ_0 as close to $90°$ as possible. (It is important to mention that the interface need not be a function at any time; the method naturally handles curves and surfaces which are not described by functions. However, our implementation cannot handle topological changes of the interface.) The initial concentration is given by

$$\tilde{C} = 1/k, \tag{A.13}$$

in the solid and

$$\tilde{C} = 1 + \frac{1-k}{k} \exp\left(\frac{-1}{|\nabla\rho(\mathbf{x})|}\right) \tag{A.14}$$

in the liquid. The last two equations translate into $c_S = c_L = 1$ at $t = 0$ in the bulk solid and liquid phases (for the original variables) by way of Eq. (A.11) and (A.1). However, at the interface (that is at $\rho(\mathbf{x}) = 0$) $C = (1+k)\tilde{C}/2$, and thus $C > 1$ since according to Eq. (A.14) $\tilde{C}$ varies between 1 and $1/k$ in the interfacial region. Initial potential is zero in both phases.

Appendix B. On smearing of the material properties across the interface

Due to the properties of the distribution function, the difference in the bulk values of the electrical conductivity, electrical mobility and diffusivity is smeared across the interface on a scale of 5–6 grid points. The isocontours of the concentration field in Fig. 3(a), and the interface shapes in Fig. 9 are rough due to numerical and interpolation errors, stemming from parameter values difference of several order of magnitude across the interface. This is particularly true in the case of Fig. 9, where this difference is pushed to a limit and the smoothing procedure of the method is incapable to satisfactory compensate for abrupt changes. In the case of Fig. 3(a), different interpolation methods produced slightly different contours in the interface vicinity, especially near regions of high curvature. For the electrical potential the problem is less acute, since the ratio of the the electrical conductivities,

Σ in Laplace equation (A.8) is not very small (0.1) for all computations (except Fig. 9, where it is smaller); however, the ratios D_L/D_S and U_L/U_S in the concentration evolution Eq. (A.7) are 10^{-2} and 3×10^{-7}, respectively (again, except Fig. 9). The numerical errors tend to accumulate slowly and they do not compromise the computation at large, at least on the time scale of computed overgrowth.

References

[1] C.C. Mitchell, M.E. Coltrin, J. Han, J. Crystal Growth 222 (2001) 144.
[2] T. Sasaki, M. Kitamura, I. Mito, J. Crystal Growth 132 (1993) 435.
[3] Y. Sakata, Y. Inomoto, K. Komatsu, J. Crystal Growth 208 (2000) 130.
[4] L. Jastrzebski, J. Lagowski, H.C. Gatos, A.F. Witt, J. Appl. Phys. 49 (12) (1978) 5909.
[5] T. Bryskiewicz, Prog. Cryst. Growth Characterization 12 (1986) 29.
[6] Yu.V. Shmartsev, Cryst. Properties Preparation 35 (1991) 173.
[7] S. Dost, H.A. Erbay, Int. J. Eng. Sci. 33 (1995) 1385.
[8] S. Dost, Z. Qin, N. Djilali, J. Crystal Growth 143 (1994) 141.
[9] New concepts and development of liquid-phase electro-epitaxy for silicon and III–V compound semiconductors, Contract DASG60-92-C-0004, AstroPower, Inc., 24 June 1995 (M.G. Mauk, PI).
[10] M.G. Mauk, J.P. Curran, J. Crystal Growth 225 (2001) 348.
[11] Z.R. Zytkiewicz, J. Domagala, D. Dobosz, J. Appl. Phys. 90 (12) (2001) 6140.
[12] D. Dobosz, Z.R. Zytkiewicz, T.T. Piotrowski, E. Kaminska, E. Papis, A. Piotrowska, Cryst. Res. Technol. 38 (3–5) (2003) 297.
[13] S. Sakai, Y. Ohashi, Y. Shintani, J. Appl. Phys. 70 (9) (1991) 4899.
[14] S. Sakai, Y. Ohashi, Jpn. J. Appl. Phys. 33 (1994) 23.
[15] D. Juric, G. Tryggvason, in: Heat Transfer in Microgravity Systems, HTD-vol. 332, ASME, 1996, p. 33.
[16] D. Juric, G. Tryggvason, J. Comput. Phys. 123 (1996) 127.
[17] S.R. Coriell, G.B. McFadden, A.A. Wheeler, D.T.J. Hurle, J. Crystal Growth 94 (1989) 334.
[18] A.A. Wheeler, S.R. Coriell, G.B. McFadden, D.T.J. Hurle, J. Crystal Growth 88 (1988) 1.
[19] A.A. Wheeler, G.B. McFadden, S.R. Coriell, D.T.J. Hurle, J. Crystal Growth 100 (1990) 1.
[20] B. Tuck, Atomic Diffusion in III–V Semiconductors, IOP Publishing Ltd., 1988.
[21] J.J. Hsieh, Liquid phase epitaxy, in: T.S. Moss (Ed.), Handbook on Semiconductors, vol. 3, North-Holland, Amsterdam, 1980, p. 415.

[22] Yu.F. Biryulin, V.V. Chaldyshev, S.V. Novikov, Yu.V. Shmartsev, Cryst. Properties Preparation 32–34 (1991) 545.

[23] J. Adams, MUDPACK: multigrid FORTRAN software for the efficient solution of linear elliptic partial differential equations, Appl. Math. Comput. 34 (1989) 113.

[24] E. Yokoyama, R.F. Sekerka, J. Crystal Growth 125 (1992) 389.

[25] C. Herring, in: W.E. Kingston (Ed.), Physics of Powder Metallurgy, McGraw-Hill, New York, 1951, p. 143.

[26] G. Tryggvason, B. Bunner, A. Esmaeeli, D. Juric, N. Al-Rawahi, W. Tauber, J. Han, S. Nas, Y.-J. Jan, J. Comput. Phys. 169 (2) (2001) 708.

[27] C.S. Peskin, J. Comput. Phys. 25 (1977) 220.

[28] M. Khenner, R.J. Braun, M.G. Mauk, J. Crystal Growth 241 (2002) 330.

[29] S. Dost, J. Su, J. Crystal Growth 167 (1996) 305.

[30] S.O. Unverdi, G. Tryggvason, J. Comput. Phys. 100 (1992) 25.

[31] M. Khenner, R.J. Braun, M.G. Mauk, J. Crystal Growth 235 (2002) 425.

[32] M. Khenner, J. Comput. Phys. 200 (2004) 1.

[33] J. Zhang, M.J. Miksis, S.G. Bankoff, Motion of a viscous drop with a moving contact line, unpublished.